Cerebellar folding is initiated by mechanical constraints on a fluid-like layer without a cellular pre-pattern

Andrew K Lawton[1], Tyler Engstrom[2], Daniel Rohrbach[3], Masaaki Omura[3,4,5], Daniel H Turnbull[4], Jonathan Mamou[3], Teng Zhang[6], J. M. Schwarz[2], and Alexandra L Joyner[1,7,*]

[1] Developmental Biology Program. Sloan Kettering Institute. New York, NY 10065, USA

[2] Department of Physics, Syracuse University, Syracuse, NY 13244, USA

[3] Lizzi Center for Biomedical Engineering, Riverside Research, NY 10038, USA

[4] Skirball Institute of Biomolecular Medicine and Department of Radiology, NYU School of Medicine, NY 10016, USA

[5] Graduate School of Science and Engineering, Chiba University, Chiba 263-8522, Japan

[6] Department of Mechanical & Aerospace Engineering, Syracuse University, Syracuse, NY 13244, USA

[7] Biochemistry, Cell and Molecular Biology Program, Weill Graduate School of Medical Sciences of Cornell University, New York, NY, 10065 USA.

[*] Corresponding author: joynera@mskcc.org, 212-639-3962

Keywords: cerebellum, development, brain folding, elastic bi-layer, wrinkling, fluid.

Abstract

Models based in differential expansion of elastic material, axonal constraints, directed growth, or multi-phasic combinations have all been proposed to explain brain folding. However, the cellular and physical processes at the time of folding have not been defined. We used the murine cerebellum to challenge the standard folding models with *in vivo* data from the time of folding initiation. We show that at folding initiation differential expansion is created by the outer layer of proliferating progenitors expanding faster than the core. However, the stiffness differential, compressive forces, and emergent thickness variations required by elastic material models are not present. We find that folding occurs without an obvious cellular pre-pattern, that the outer layer expansion is uniform and fluid-like, and that the cerebellum is under radial and circumferential constraints. Lastly, we find that a multi-phase model incorporating differential expansion of a fluid outer layer and radial and circumferential constraints approximates the *in vivo* shape evolution observed during initiation of cerebellar folding. We discuss how our findings provide a new mechanistic framework to understand brain folding.

Recent work to elucidate the mechanics of in brain folding has primarily focused on the human cerebral cortex and involved models of directed growth, axonal tension, or differential expansion of elastic materials that generate compressive forces to drive mechanical instabilities leading to folding (1-8). Current elastic material models are able to create three-dimensional shapes strikingly similar to the final folds seen in the adult human cortex (9). A recent multi-phase model (10) that includes elastic and fluid-like layers, differential expansion and radial constraints takes into consideration that multiple factors could lead to folding in the developing brain. However, the cell and tissue level mechanics actually present at the initiation of folding have not been considered or defined, as technological limitations are significant in animals with a folded cerebrum.

The murine cerebellum has a simple alignment of 8-10 stereotypical folds along the anterior-posterior axis. Combined with the genetic tools available in mouse this allows for precise developmental interrogation to identify and analyze the *in vivo* cellular and tissue level behaviors driving growth and folding. The developing cerebellum is distinct from the cerebral cortex, as it has a temporary external granule cell layer (EGL) of proliferating granule cell precursors that cover the surface and generate growth primarily in the anterior-posterior (AP) direction (11-13). During development a thickening occurs in the EGL at the base of each forming fissure, termed anchoring center (AC) (14), whereas in the adult cerebellum the inner granule cell layer (IGL), generated by the EGL during the first two weeks of life, is thinnest at the ACs. Previous work on cerebellar folding utilized a tri-layer elastic model incorporating the EGL, the adjacent molecular layer, rich in axons and dendrites, and the IGL (7). However, neither the molecular layer nor the IGL are present when folding is initiated in the embryo. Therefore we argue that a bilayer system

consisting of the EGL and underlying core, is a more appropriate approximation for cerebellar folding.

Here we show that cerebellar folding emerges from differential expansion between an un-patterned, rapidly expanding EGL and an underlying core. Additionally, we demonstrate that the measured stiffness differential, compressive forces, and the thickness variation in the EGL are all inconsistent with traditional elastic wrinkling models driven by differential growth. Furthermore, we demonstrate that the expansion of the EGL is uniform, and fluid-like, and that the cerebellum is under radial and circumferential constraints when folding initiates. Lastly, we constrain the recent multi-phase model with our *in vivo* data and find we can capture the temporal shape evolution seen during mouse cerebellum folding initiation. The implications of our findings for human cerebral cortex folding are discussed.

Tissue level mechanics drive folding

It is well known that differentially expanding bilayer systems can wrinkle to relax building stress (15-19). We reasoned that in the cerebellum the EGL could behave as a quickly expanding outer layer and its attachment to a more slowly growing core could generate forces that result in a wrinkling-like phenotype. To test whether the cerebellum has differential expansion between the two layers, we measured the expansion of the EGL and the core during the time of initiation of folding from midline sagittal sections (Fig 1a-d). Unlike the cerebral cortex, the unfolded murine cerebellum is a simple cylinder-like structure elongated in the medio-lateral axis (Fig. 1e) (20). All folds in the medial cerebellum (vermis) are aligned in the same axis allowing 2-D measurements to estimate expansion in the anterior-posterior axis of the vermis. Therefore the

length of the surface of the EGL was used as a measure of the cerebellum surface area and the area of the core as an approximation of cerebellum volume (Fig. 1d), and measurements were made each day from embryonic day 16.5 (E16.5) through postnatal day 0 (P0). In cross-section the unfolded cerebellum approximates a semicircle, therefore we reasoned that if the cerebellum were to remain unfolded then the ratio of expansion between the length of the EGL and the area of the core should approximate the ratio of the circumference of a semi-circle to its area. Of significance, we found that at E16.5 and E17.5 the ratios of growth between the EGL and core closely approximated the expansion of a semi-circle. However, at E18.5 and P0 the expansion rate of the EGL was greater than the rate of core expansion (Fig. 1f). Thus we uncovered that the cerebellum does indeed go through a phase of differential expansion. We next determined whether differential expansion correlates with when folding occurs by calculating a folding index (the convex curvature of the EGL divided by the length of the EGL) at each stage (21). Indeed, we found that the cerebellum remains unfolded during the initial proportional expansion between the EGL and core and only folds when the differential expansion is initiated (Fig. 1g). These results provide quantitative evidence that cerebellar folding involves tissue level mechanical forces arising from differential expansion.

In vivo data contradict elastic bilayer models

Since there is differential expansion between the EGL and the core and as this type of expansion is the driver of elastic bilayer models we tested whether the properties of cerebellar tissue are consistent with the requirements and predictions of such models. Briefly, the initial resulting wrinkling instability defines the distance between folds as the initial sinusoidal undulations increase in amplitude to ultimately turn into lobules. The folding wavelength depends on the

101 thickness of the external layer (EGL) and the ratio of the stiffness of the two layers (EGL/core).
102 In particular, for a planar geometry, with the stiffness of the external layer defined as E_o, the
103 stiffness of the core as E_i, and the thickness of the external layer denoted as t, the folding
104 wavelength λ is given by (22)

105 $$\lambda = 2\,\pi\,t\,\left(\frac{1}{3}\frac{E_o}{E_i}\right)^{1/3}.$$

106 If the length of the system is l, then the number of folds is inversely proportional to the thickness
107 of the EGL

108 $$n = \frac{l}{\lambda} \propto \frac{l}{t}\left(\frac{E_i}{E_o}\right)^{1/3}.$$

109 We explored a standard elastic bilayer model in a circular geometry using the observed ratio of
110 thickness of the EGL to radius of the cerebellum near the onset of shape change (E16.5) and
111 invoked a neo-Hookean elastic solid for both layers (23). The resulting shape change was studied
112 as a function of the ratio of the layer stiffness values (Fig. 2a). We found that to produce the
113 observed number of folds (three in the semi-circular cerebellum and 6 in the circular model) at
114 initiation of folding through wrinkling based models constrained by our measurements of the
115 embryonic cerebellum, a large stiffness ratio was required of around 50. To map the stiffness
116 contrast in the cerebellum we used scanning acoustic microscopy to measure the bulk modulus of
117 the cerebellum daily from E16.5 to P18.5 (Fig. 2b-c, Supplemental Fig. 1). For small
118 deformations, we expect the instantaneous bulk modulus to be linearly related to the stiffness
119 and, therefore, the ratio of the instantaneous bulk moduli should scale similarly to the ratio of
120 stiffnesses (assuming the same Poisson's ratio for the EGL and for the core, neither of which
121 have been directly measured). While this qualitative approach may not be able produce the
122 absolute values of the elastic properties of the tissues, it can give a reasonable indication of the

stiffness of different parts in the cerebellum. Using this estimation, we found that the EGL has a slightly higher instantaneous bulk modulus than the core at all stages measured. Unsurprisingly, the ratio (~1:1.05) was not close to being sufficient to produce a folding wavelength similar to that in the cerebellum (Fig. 2d). Consistent with our finding, small modulus contrasts have been reported for other brain regions with multiple loading modes, such as shear, compression, and tension (4,7,24). Elastic material models with graded growth profiles have been developed that predict folding of cerebral cortex without a large stiffness differential (1). However, these models are still bound by other measurable requirements as discussed below.

Elastic bi-layer wrinkling models predict compressive forces in the outer layer. Simulations performed of cuts through the outer layer and into the inner layer predict that upon relaxation the outer layer should not open (Fig. 2e). We tested whether this prediction reflects the biology using surgical dissection blades to make radial cuts across the meninges, EGL, and into the core of live E16.5 tissue slices. Time-lapse imaging revealed that, in contrast to the prediction, the EGL opens as well as part of the underlying cut in the core (Fig. 2f-h, Supplemental Fig. 2a-c, and Supplemental Movie 1). This result indicates there is circumferential tension within the outer layers of the cerebellum. This finding also rules out the elastic models with graded growth profiles as they predict compressive forces in outer region as well.

The elastic bi-layer model requires the EGL to be thinnest at the base of each AC, which are the lowest parts of the cerebellar surface. Thus, the EGL should have an “in-phase” thickness variation. Without this feature, a purely elastic model – bi-layer based or even graded growth profile based – cannot be in mechanical equilibrium (in the quasistatic limit). However, we previously reported that the embryonic EGL is thickest in the ACs when folding initiates, i.e., it

146 has an “out-of-phase” thickness variation (14). To validate this observation, we quantified the
147 thickness variations in the EGL centered at the ACs present at E16.5-18.5. Not all cerebella have
148 visible AC at E16.5. However in the subset that do and in the three ACs present at E17.5, the
149 EGL was found to be 1.2 – 1.4 times thicker in the ACs than in the surrounding EGL (Fig. 2i-l
150 and Supplemental Fig. 3). Moreover, the thickness ratio increased to 1.7 times at E18.5 (Fig 2l).
151 As described above, the final thickness variations of the IGL (as well as the molecular layer) of
152 the cerebellar cortex are in-phase, just as the layers of the adult cerebral cortex. These results
153 further show that traditional elastic wrinkling models cannot capture the initiation of cerebellum
154 folding, and highlight the importance of making biological measurements at the time of folding
155 rather than when it is complete.
156
157 **Uniform outer layer expansion without a cellular pre-pattern**
158 As elastic bi-layer models do not align with the biology of cerebellar folding, we looked for
159 other drivers of morphometric changes. Since the EGL drives the majority of cerebellar growth
160 (11-13), we first tested whether regional differences in EGL proliferation rates are present that
161 could influence the folding pattern of the cerebellum. Proliferation rates (S phase index) were
162 measured in the EGL during folding initiation (E16.5 and E17.5) in the inbred FVB/N strain to
163 reduce variation between samples. First we asked if the regions that will give rise to distinct sets
164 of lobules have different rates of proliferation that could contribute to the larger and smaller sizes
165 that the lobules ultimately attain. We focused on the anterior cerebellum that divides into a larger
166 region with lobules 1-3 (L123) and smaller region (L45), as well as the central area that
167 comprises lobules 6-8 (L678) of the cerebellum (Figure 3a-b). The more posterior cerebellum
168 does not consistently fold at this stage, thus measurements were not included. Interestingly, we

169 found that the proliferation rates were similar in the three regions at E16.5 (Fig. 3c). The EGL
170 proliferation rate at E17.5 in L678 was slightly reduced compared to the L123 region, but no
171 other differences were found (Fig. 3d). Thus proliferation is uniform just before initiation of
172 folding and the small difference found during folding does not correlate with lobule size. This
173 result indicates that lobule size is not determined by modulating the levels of proliferation at the
174 onset of folding. Rather, lobule size could be set by both the timing of invagination, and the
175 distance between ACs as granule cell precursors in one lobule do not cross the surrounding ACs
176 to contribute to an adjacent lobule (12).
177
178 Each AC is first detected as a regional inward thickening of the EGL (14) (Fig 2i-l and
179 Supplemental Fig.3). We measured the proliferation of the EGL specifically within the forming
180 AC regions to test whether altered proliferation rates could explain the thickenings and therefore
181 the initiation of an AC. We found the rate of proliferation within each forming AC region at
182 E16.5 and E17.5 was the same as in the surrounding EGL (Fig. 3e,f), thus proliferation within all
183 regions of the EGL at the initiation of folding is uniform. Furthermore, regional modulation of
184 proliferation does not form or position the ACs.
185
186 At E18.5, after the initiation of folding, we found that the rate of proliferation was significantly
187 lower in the L678 region compared with the L123 and L45 regions (Supplemental Fig. 4a).
188 However, proliferation within the ACs at E18.5 remained uniform with the surrounding regions
189 (Supplemental Fig .4b). Since ACs compartmentalize the EGL, our results show that regional
190 differences in proliferation rates arise in lobule regions after initiation of folding, which thus
191 could be important for determining the ultimate size of the folds.

192

193 Changes in cell size and shape have been shown to induce morphological changes (25-28). To
194 test if regionally specific regulation of cell shape or size directs folding, we fluorescently labeled
195 cell membranes of scattered granule cell precursors (GCPs) in the EGL using genetics (*Atoh1-*
196 *CreER/+; R26*$^{MTMG/+}$ mice injected with tamoxifen two days prior to analysis). We then
197 segmented the cells in 3D and quantified their sphericity (Fig. 3g). We discovered that GCPs in
198 the EGL take on a large variation of shapes and sizes at E16.5 and E18.5. However, we found no
199 difference in cell shape in the different lobule regions of the EGL or between the AC areas and
200 the surrounding EGL at each age (Fig. 3h,i). Cell size was uniform at both stages except for a
201 slight reduction in L678 at E16.5 when compared with L123 and the AC regions. However, the
202 size of cells is reduced at E18.5 compared to E16.5 (Fig 3 j,k and Supplemental Fig 4c). Thus,
203 the proliferating GCPs that drive expansion of the EGL have both uniform proliferation rates and
204 similar shapes and sizes across the lobule regions defined by the first three ACs at folding
205 initiation.

206

207 **Uniform fiber distribution and radial tension at folding initiation**

208 The EGL is traversed by fibers of Bergmann glial and radial glial cells (29-31). We tested
209 whether the fibers are distributed in patterns that could locally change the physical properties of
210 the EGL and induce invaginations. Genetics was used to fluorescently label cell membranes of
211 scattered glial cells (*nestin-creER/+;R26*$^{MTMG/+}$ mice injected with tamoxifen at E14.5) (Fig 4a).
212 Fibers crossing the EGL at E16.5 were counted in sagittal slices and aligned relative to the ACs
213 (Fig. 4b). This analysis showed that the Bergmann glial and radial glial fibers are distributed

214 evenly along the AP axis of the EGL, and therefore are not directing the positions where folding
215 initiates based on an uneven regional distribution.
216
217 Tension based folding models suggest constraints from axons and other fibers could direct
218 folding (4, 32). Since the cerebellum is under circumferential tension, as demonstrated above, we
219 examined evidence of radial tension between the EGL and the ventricular zone (VZ) at the
220 initiation of folding. Cuts were made in live E16.5 tissue slices between the EGL and VZ
221 running approximately parallel to them so that they cut across radial fibers in the anterior
222 cerebellum (Fig 4c). As predicted, after cutting the tissue relaxed revealing tension directed
223 radially within the cerebellum (Fig. 4d,e and Supplemental Fig 2 and Supplemental Movie 2).
224 Interestingly, quantification of how the radial and horizontal cuts open revealed that only the
225 horizontal cuts opened along the full length of the cut although they opened more slowly than
226 radial cuts (Supplemental Fig 2g-j), indicating different stress profiles in the two orientations.
227
228 Taken together, at the time of folding initiation the EGL, which is driving the differential
229 expansion, is itself growing uniformly and the cerebellum is under both radial and
230 circumferential constraints. Finally, there is no evidence of any pre-patterning in the EGL in
231 either cellular behaviors or fiber distribution.
232
233 **The EGL is fluid-like as cells undergo dynamic rearrangement**
234 As the granule cells within the EGL have such varied shapes as shown above, we looked to see if
235 the cells within the EGL were undergoing any rearrangement movements that may indicate fluid
236 properties. A small, scattered fraction of nuclei in the EGL were fluorescently labeled (*Atoh1-*

237 *CreER/+; R26*$^{Ai75/+}$ injected with tamoxifen two days prior to imaging) and *ex vivo* slice-culture
238 time-lapse imaging was performed for up to five hours. Tracking the cell positions through time
239 revealed that granule cells within the EGL are highly motile within the EGL. Furthermore, there
240 was no obvious directionality or collectivity to the movement. However, the dynamic motility
241 resulted in the constant exchanging of nearest neighbors over the course of tens to hundreds of
242 minutes and shows that at the timescale of folding the EGL is more fluid-like than a solid
243 epithelial layer (Figure 5 and Supplemental Movies 3 and 4).
244
245 **Multi-phase wrinkling model simulates cerebellar shape change during folding initiation**
246 We recently developed a model for folding from differentially expanding bi-layer tissues that
247 takes into account the out-of-phase thickness of the outer layer of several systems and possible
248 contribution of radial mechanical constraints present in neurological tissue (10). We applied the
249 model here to the initiation of cerebellar folding based on five primary assumptions. First, the
250 core is an incompressible material (μ) as indicated by the bulk modulus measurements. Second
251 the outer layer, i.e. the EGL, expands uniformly (k_t) as shown by the proliferation rate. Third, the
252 EGL is assumed to be a fluid-like material as demonstrated by the live-imaging of neighbor
253 exchanges. Fourth, there is an elastic component radially to the entire cerebellum (k_r), seen in the
254 cutting and relaxation experiment and possibly mediated by radial glia. Fifth, the EGL is
255 constrained towards a uniform thickness (β), possibly by Bergmann glia fibers spanning the
256 EGL. Given the interplay between incompressible material, compressible fibrous material, and a
257 proliferating non-elastic EGL, this model is multi-phase.
258

An energy functional parameterized by both the inner and outer boundary of the EGL and incorporating the above five assumptions into three dimensionless parameters (μ/k_r, k_r/k_t, k_t/β) is minimized to yield an equation for a driven harmonic oscillator resulting in sinusoidal shapes for both the inner and outer boundary of the EGL given an initial elliptical shape. In contrast with the elastic bilayer wrinkling model, EGL thickness oscillations are found to be out-of-phase with the surface height (radius) oscillations when $0 < \mu/k_r < 1$. Additionally, the model predicts that the ratio of the measured surface height amplitude (A_r) and the EGL thickness amplitude (A_t) is given by

$$\frac{A_r}{A_t} = \frac{\frac{\mu}{k_r}}{1 - \frac{\mu}{k_r}} ,$$

which need not be $\gg 1$ as is typical of elastic bilayer wrinkling, and the number of initial folds at E16.5 is determined by

$$n = \sqrt{\frac{k_t}{\beta}} \sqrt{1 + \frac{\frac{\mu}{k_t}}{1 - \frac{\mu}{k_r}}} .$$

Note that in contrast with elastic wrinkling, the number of initial folds does not depend on the thickness (a length scale) of the EGL, but only on material properties.

Given that our tissue cutting and relaxation experiment revealed circumferential tension in the cerebellum at folding initiation (Fig. 2f-h, Supplemental Movie 1), we returned to the mathematics and found a previously unrealized geometric relationship in the circular limit of the model that in fact assumes circumferential tension in addition to the previously discussed radial tension given that the perimeter of a circle is determined by its radius.

280 To rigorously test the shape prediction of the model, we first constrained 3 of the 5 parameters
281 for a circular version of the model by using both the thickness amplitude, and average thickness
282 of the EGL, as measured at E16.5, and the number of initial folds. Secondly, the parameter μ/k_r
283 (denoted as ε) was assumed to scale linearly with time. Together, this allowed for the generation
284 of shape predictions at later developmental stages (E17.5 and E18.5) from the E16.5 starting
285 approximation. Solving the numerical model as constrained by our measured embryonic data we
286 found that it closely approximates the phase and amplitude behavior of EGL thickness and radius
287 oscillations from E16.5 through E18.5. (Fig. 6a-c). However, the model is not able to produce
288 self-contacting folds or hierarchical folding, both of which are seen in the cerebellum at later
289 stages.
290
291 **Hierarchical folding involves differential growth**
292 The cerebellum has hierarchical folding in which the initial folds become subdivided. Given that
293 ACs hold their position during development and compartmentalize granule cells within lobules
294 of the EGL (12) we reasoned that the ACs could be acting as mechanical boundaries enabling
295 similar mechanics to drive the secondary folding. To test this possibility we measured the
296 expansion of the EGL and the core of the individual lobule regions from E18.5 to P3. We found
297 that indeed in the lobule regions that undergo folding there is a temporal correlation between
298 when the onset of sub-folding and differential expansion occur (Supplemental Fig. 5a-d). In
299 contrast, the region (L45) that does not fold during the same time period has a different, more
300 rectangular shape, and the ratio of EGL growth to core growth is proportional for a rectangle
301 during the time measured (Supplemental Fig. 5).
302

Discussion

Here we have provided experimental evidence that cerebellar folding emerges without obvious pre-patterning. Additionally, the outer layer has fluid-like properties and expands uniformly, and the growth creates a differential expansion between the outer layer and the core. Thus, traditional morphometric cellular behaviors such as changes in cell shape, size and proliferation do not direct where cerebellar folding initiates. Furthermore, our developmental interrogation revealed tissue moduli, mechanical constraints, and emergent thickness variations in the EGL that are fundamentally inconsistent with traditional elastic bilayer wrinkling models. Therefore our results call for a new understanding of brain folding.

By applying a multi-phase model constrained by our measured data we were able to capture the correct shape variations and number of folds at the onset of folding. Our new framework accounts for: the rapidly expanding fluid EGL, whose thickness is proposed to be regulated by Bergmann glial fibers, the slower growing incompressible core, and fibrous material in the form of glial fibers and possibly axons as well as the meninges that potentially provide radial and circumferential tension (Supplemental Fig. 6). This multi-phase model of folding makes many new predictions. One such prediction is that adjusting the amount of tension spanning the cerebellum will change the degree of folding. Indeed, alterations of the cells that likely create tension-based forces could explain the dramatically disrupted folding seen in mouse mutants in which radial glia do not produce Bergmann glia (33). Without Bergmann glia, the EGL would be expected to not form a layer with regular thickness and it should be more sensitive to variations in radial glial tension. Consistent with this prediction, mutants without Bergmann glia have more

325 localized and less regular folds (34). Our combination of experimental studies and modeling thus
326 provide new insights into cerebellar folding, including an underappreciated role for tension.
327
328 Under the new framework revealed by our measurements made in the developing mouse
329 cerebellum, to approximate the observed shape changes in the murine cerebellum from E17.5 to
330 E18.5 the ratio of the core stiffness over the radial tension must increase. Yet, the measured bulk
331 modulus of the core shows no increase during development. Therefore a second prediction is that
332 radial tension must decrease during development. While the cerebellum is crossed by many
333 fibers at folding initiation, radial glial fibers are an attractive candidate to mediate this change in
334 radial tension (34, 35). First, they span from the VZ to the surface of the cerebellum at E16.5.
335 Additionally, during folding initiation the radial glia undergo a transition into Bergmann glia
336 where they release their basal connection to the VZ and the cell body migrates towards the
337 surface (21). This transition could lead to a reduction in the global radial tension and thus would
338 be consistent with our model prediction.
339
340 The mechanics underlying hierarchical folding remain an open challenge. However, our
341 developmental data may provide a way forward. As ACs maintain their spatial positions, and as
342 they compartmentalize granule cells within the EGL into the lobule regions (12), we propose that
343 they create fixed mechanical boundaries that divide the cerebellum into self-similar domains.
344 These domains, with their similar physical properties to the initial unfolded cerebellum, can then
345 undergo additional folding. Furthermore since ACs compartmentalize granule cells within the
346 lobule regions, once separated the lobule regions can develop distinct characteristics, like the
347 observed differential proliferation rates at E18.5. We speculate, therefore, that the folding

348 patterns seen across cerebella in different species evolved by adjustment of global as well as
349 regional levels of differential expansion and tension which ultimately mold the functionality of
350 the cerebellum.
351
352 Finally it is interesting to note the similarities and differences between the developing
353 cerebellum and the cerebral cortex. Radial glia span the entire cerebral cortex just as in the
354 cerebellum (36). Furthermore, species with folded cerebrums have evolved outer radial glial cells
355 for which the cell body leaves the ventricular zone and to become positioned near the surface
356 while retaining fibers anchored on the surface, similar to Bergmann glia in the cerebellum (29,
357 37). While we have emphasized the notion of tension via glial fibers in the developing
358 cerebellum, axonal tension has been discussed in the context of shaping the developing cerebrum
359 (32). Tissue cutting in the cerebral cortex of ferrets has revealed a similar tension pattern during
360 folding as we found in the cerebellum (4). We therefore submit that our work calls for a revival
361 of the notion of how tension affects the shape of the developing cerebrum.
362
363 Unlike the cerebellum, the cerebral cortex is not divided into a simple bilayer system. However,
364 outer radial glial cells proliferate, much like the GCPs of the EGL, to drive the expansion of the
365 outer regions of the cerebral cortex around the time of initiation of folding (38-40). Moving the
366 zone of proliferation out from the VZ gives more space for the increased proliferation required in
367 folding systems. The cerebellum, housing 80% of the neurons in the human may be an extreme
368 example requiring the region of proliferation to be completely on the outer surface (41).
369 Constraining models of folding of different brain regions with developmental data will bring
370 about a more accurate quantitative understanding of the shaping of the developing brain.

371

372 **Materials and Methods**

373 All experiments were performed following protocols approved by Memorial Sloan Kettering
374 Cancer Center's Institutional Animal Care and Use Committee. All materials and methods used
375 to support this study are described in SI Materials and Methods.

376

377 **Acknowledgements** We are grateful to Anna-Katerina Hadjantonakis and Songhai Shi for use of
378 Imaris software. We thank Jennifer Zallen and Anna-Katerina Hadjantonakis for experimental
379 advice, Nathanael Kim for help with the acoustic microscopy and Professor Tadashi Yamagushi
380 for his support for MO's visit to New York. We appreciate the discussions we have had with
381 Alexandre Wojcinski and the entire Joyner Laboratory, and the administrative support from Cara
382 Monaco. This work was supported by grants from the NIH to A.L.J. (R37MH085726 and
383 R01NS092096) and A.K.L. (F32 NS086163) and a National Cancer Institute Cancer Center
384 Support Grant (P30 CA008748-48). T.A.E. and J.M.S. acknowledge financial support from NSF-
385 DMR-CMMT Award Number 1507938 and NSF-PHY-PoLS Award Number 1607416. FE
386 simulations were performed at the Comet cluster (Award no. TG-MSS170004) in XSEDE. The
387 development of the acoustic microscopy instrument and signal-processing methods was
388 supported by NIH grant R21EB016117 awarded to J.M.

389

390 **Author Contributions**

391 A.K.L. and A.L.J. conceived the project; T.E., T.Z. and J.M.S. designed and performed the
392 modeling, A.K.L and A.L.J. designed the experimental research; A.K.L performed the
393 experiments; D.R., M.O., J.M. and D.T. performed the acoustic microcopy experiments and

394 analyzed the data; all authors discussed the data; A.K.L. and A.L.J. wrote the manuscript with
395 contributions from all authors.
396
397 **Competing Interests** The authors declare no competing interests.
398 **Correspondence and requests for materials** should be addressed to A.L.J.
399
400 **Materials and Methods**
401 **Animals.**
402 The inbred FVB/N stain was used for all proliferation rate, area, length, and expansion rate
403 measurements. *Atoh1-CreER* (42), *Nestin-CreER* (43), *Rosa26*^{MTMG} (44) , *Rosa26*^{Ai75} (45) were
404 used to quantify cell shape and size as well as fiber distribution and were maintained on the
405 outbred Swiss Webster background. The Swiss Webster strain was used for scanning acoustic
406 microscopy. Both sexes were used for the analysis. Animals were kept on a 12 hour light/dark
407 cycle and food and water were supplied ad libitum. All experiments were performed following
408 protocols approved by Memorial Sloan Kettering Cancer Center's Institutional Animal Care and
409 Use Committee.
410
411 The appearance of a vaginal plug set noon of the day as Embryonic day 0.5 (E0.5). All animals
412 were collected within two hours of noon on the day of collection. Tamoxifen (Tm, Sigma-
413 Aldrich) was dissolved in corn oil (Sigma-Aldrich) at 20 mg/mL. Pregnant females carrying
414 litters with *Atoh1-CreER/+;R26*$^{MTMG/MTMG}$ or *NestinCER/+;R26*$^{MTMG/MTMG}$ embryos were given
415 one 20 µg/g dose of TM via subcutaneous injection two days prior to analysis. 25 µg/g of 5-

416 ethynyl-2-deoxyruidine (EDU; Invitrogen) was administered via subcutaneous injection one hour
417 prior to collection.
418
419 **Tissue processing, immunohistochemistry, and Imaging**
420 For embryonic stages heads were fixed in 4% paraformaldehyde overnight at 4°C. For postnatal
421 animals, the brain was dissected out first before fixation. Tissues were stored in 30% sucrose.
422 For all proliferation, area, length, and thickness measurements brains were embedded in optimal
423 cutting temperature (OCT) compound. Parasagittal sections were collect with a Leica cryostat
424 (CM3050s) at 10µm.
425
426 Prior to IHC, EdU was detected using a commercial kit (Invitrogen, C10340). Following EdU
427 reaction the following primary antibodies were used either overnight at 4°C or 4 hours at room
428 temperature: mouse anti-P27 (BD Pharmingen, 610241), rabbit anti-GFP (Life Technologies,
429 A11122), rat anti-GFP (Nacalai Tesque, 04404-84). All antibodies were diluted to 1:500 in 2%
430 milk (American Bioanalytical) and 0.2% Triton X-100 (Fisher Scientific). Alexa Fluor secondary
431 antibodies (1:500; Invitrogen) were used: Alexa Fluor 488 donkey anti-rabbit, A21206, Alexa
432 Fluor 488 donkey anti-rat, A21208, Alexa Fluor 488 donkey anti-mouse, A21202, Alexa Fluor
433 647 donkey anti-mouse, A31571. EdU was detected using a commercial kit (Invitrogen,
434 C10340).
435
436 For cell size, shape and fiber density analysis 60 µm parasagittal sections were collected on a
437 Leica vibratome (VT100S). Primary and secondary antibodies were diluted 1:500 in 2% milk
438 and incubated overnight at 4°C.

439

440 For scanning acoustic microscopy brains were processed for paraffin embedding and parasagittal
441 sections of 10 µm thick were collected on a microtome (Leica RM2255). Structured illumination
442 and confocal Imaging was done with Zeiss Observer Z.1 with Apatome or Zeiss LSM 880
443 respectively.

444

445 **Quantification of Proliferation, Length, Area, Folding Index and Thickness**

446 Measurements for all analysis were taken from the three most midline sagittal sections and
447 averaged. The most midline section was determined by dividing the distance in half between the
448 lateral edges where the third ventrical and the mesencephalic vesicle are no longer connected.
449 Quantifications were made using Imaris (Bitplane) and Matlab (Mathworks) software.

450

451 EGL Proliferation rate was calculated as EDU+/(Dapi+;P27-) cells. All cells were counted
452 within the lobule region to the midpoint of the Anchoring Centers. For proliferation
453 measurements through the ACs and the surrounding EGL at E16.5 and E17.5 a 50 µm window
454 measured from the outer surface of the EGL was centered at the AC. The measuring window was
455 centered at every 25 µm anterior and posterior to the EGL for a total distance of 250 µm anterior
456 and posterior to the AC. At E18.5, when the AC is fully formed, everything proximal to the
457 centroid of the cerebellum under the midpoint of the AC was counted as the AC. Non-
458 overlapping regions of 50 µm also were measured in either direction for a total of 200 µM
459 anterior and posterior to the AC. Proliferation was measured in 3 cerebella at E16.5 and E17.5
460 and in 4 cerebella at E18.5

461

462 EGL length was measured from the outer surface of the EGL following the curvature of the
463 EGL. Cerebellar area was calculated as the area within the outer surface of the EGL and the
464 ventricular zone. A short strait edge was made perpendicular to the ventricular zone to close the
465 area back upon to the anterior end of the EGL. The convex curvature of the cerebellum was
466 measured by following only the positive curvature of the EGL. The folding index was
467 determined as FI = 1 - (Positive curvature/EGL length). Data collected for E16.5, E17.5, E18.5
468 and P0 came from 6,8,7, and 9 cerebella respectively.
469 EGL thickness was measured by defining the outer and inner curvature of the EGL. The shortest
470 distance lines were drawn to the outer curvature from discrete points distributed at every 12.5 µm
471 along the inner curvature of the EGL. Nine ACs and surrounding regions from five cerebella
472 were quantified at E16.5 and 13 ACs from five cerebellar were analyzed at E17.5. At E18.5 six
473 ACs from two cerebellar were quantified.
474
475 **Quantification of Cell Shape**
476 Midline sections were imaged with a Zeiss LSM 880. Serial images were taken to cover the
477 entire EGL of lobule regions L123, L45, and L678 and the ACs. Manual cell masks were created
478 with Imaris software defining the curvature at every z-slice. Every cell that was completely
479 included in the imaging window and that was distinguishable from surrounding cells was
480 counted to reduce sampling bias. Cells from three brains were measured at each stage for a total
481 of 131 at E16.5 and 201 at E18.5. Shape was defined via sphericity, which is the surface area of
482 a sphere having the same volume as the cell of interest divided by the surface area of the cell of
483 interest.
484

485 **Quantification of Fibers within the EGL**

486 Midline sections were imaged with a Zeiss LSM 880. Image tiling was used to cover the EGL.
487 Using Python, a 4th or 5th order polynomial was fitted to the outer edge of the EGL in each
488 image, and five scan lines were positioned at 12.2 µm intervals beneath the surface, and parallel
489 to it. A bin width of 50 µm as measured along the polynomial contour was centered at the AC.
490 Bins of equal distance were extended both anteriorly and posteriorly. Staining intensity was
491 counted along each scan line at every z-slice of the confocal stack. Each image was normalized
492 to the mean intensity and smoothed with a Gaussian filter. Peak counting was done using
493 minimum and maximum filters, keeping neighborhood size and threshold parameters constant
494 for all datasets. The results from the 5 scan lines were averaged.

495

496 **Tissue cutting**

497 Live cerebella of E16.5 FVB/N mice were collected in dissection buffer as previously described
498 (46) and embedded in low-melting point agarose (Invitrogen). Sagittal slices at a thickness of
499 250 µm were collected. Slices were removed from the agarose and place in petri-dishes coated
500 with Poly(2-hydroxyethyl methacrylate)(Sigma-Aldrich). Tissue cuts were made with a 30°
501 Premier Edge stab knife (Oasis Medical). Slices were allowed to relax for 10 minutes. Time-
502 lapse images were acquired on a Leica MZ75 dissection scope.

503

504 **Live Imaging Analysis**

505 Live cerebella of E16.5 Atoh1-CreER/+; R26Ai75/+ mice were collected and slices of a
506 thickness of 250 µm were cultured on Millicell cell culture inserts (Millipore) in glass bottom
507 plates (Matek) as previously described (46). Image stacks were acquired on a Zeiss LSM 880 at

508 intervals of around 3.5 minutes for up to 5 hours. Cell positions were tracked using Imaris
509 (Bitplane) software.
510
511 **Scanning Acoustic Microscopy**
512 Mechanical tissue properties were analyzed using a 250 MHz Scanning Acoustic Microscope
513 (SAM), described previously (47, 48). Briefly, 12 μm paraffin sections of mouse embryonic
514 brains were de-parafinized, hydrated in de-ionized water and scanned on the SAM to generate
515 maps of amplitude, sample thickness, speed of sound, acoustic impedance, attenuation, bulk
516 modulus, and mass density. Co-registered histology and SAM amplitude images were used to
517 identify regions-of-interest (ROIs) corresponding to the EGL layer and underlying core of the
518 cerebellum in each sample. Bulk modulus was analyzed as a measure of tissue stiffness: ROI
519 measurements were acquired from 3 sections from 3 embryos at each developmental stage.
520
521 **Finite element simulations**
522 The wrinkle of a circular bilayer structure in Fig. 3a was simulated with commercial software
523 ABAQUS. Both film and substrate were modeled as incompressible neo-Hookean materials. The
524 ratio between shear moduli of the film and substrate was 50 and the initial radius of the
525 simulated structure was 16 times that of the film thickness. The differential growth of the EGL
526 and core was modeled by an isotropic expansion of the film in the bilayer structure.
527
528 To test the elastic wrinkling model, we conducted finite element (FE) simulations for bilayer
529 structures with a film bonded on a substrate, which represents the EGL layer and core structure,
530 respectively. The structures were assumed to be under 2D plane strain deformation to mimic the

quasi-2D nature of cerebellum wrinkles. Neo-Hookean model was adopted to describe the elastic properties of both film and substrate, whose strain energy can be expressed as

$$U = \frac{1}{2}\mu(I_1 - 3)$$

where μ is the shear modulus and I_1 represents the first invariant of the right Cauchy-Green strain tensor. The Poisson's ratios for the film and substrate were set to be 0.5, based on experimental observations that the bulk modulus of EGL and core are in the order of GPa, much larger than the shear modulus of soft tissues (~ kPa).

We carried out FE simulations through commercial software ABAQUS. A second order 6 node hybrid element (CPE6MH) was utilized to discretize the film and substrate. Very fine FE meshes were used to make sure the results independent of mesh size. To incorporate differential growth in real EGL layer and core, an isotropic growth deformation tension was applied to the modeled film by decoupling the deformation tenor $\boldsymbol{F}$ into elastic deformation part $\boldsymbol{A}$ and growth part $\boldsymbol{G}$.

$$\boldsymbol{F} = \boldsymbol{A} \cdot \boldsymbol{G}$$

For simplicity, we assume the growth part is isotropic and controlled by a scalar variable g

$$\boldsymbol{G} = g\begin{bmatrix} 1 & 0 & 0 \\ 0 & 1 & 0 \\ 0 & 0 & 1 \end{bmatrix}$$

where $g > 1$ represents a faster growth in EGL than the core. To trigger instabilities in numerical simulations, random perturbations (e.g., White Gaussian noise with $0.001t$ mean magnitude) were applied to the nodal positions at the top surface of the film and the interface between the film and substrate.

To qualitatively understand the cut experiments we ran a FE simulation of a pre-cut circular bilayer structure and then assigned swelling strain to the film. This neglected the dynamical

process in the real cut experiments and only focused on the final equilibrium of the cerebellum after long time relaxation. All the simulation parameters were the same as those in the wrinkling simulation. The initial cut length *a* is equal to 8*t*. The minimum in-plane principal stress corresponds to the hoop stress in the film.

Details of multi-phase model as applied to initiation of cerebellar folds

We, formulated a two-dimensional model based on the parameters of a midsagittal section of the cerebellum. The distance of the outer edge of the EGL and, hence, the outer edge of the cerebellum from the center of the cerebellum was defined as r(θ) with θ as the angular coordinate. We assumed that r(θ) was single-valued. The thickness of the EGL was defined as t(θ). See model schematic below.

Taking into account the four assumptions discussed in the main text, we constructed the following energy functional to be minimized

$$E\left[r, t, \frac{dt}{d\theta}\right] = \int d\theta \, \{k_r(r - r_0)^2 - k_t(t - t_0)^2 + \beta \left(\frac{dt}{d\theta}\right)^2\},$$

with k_r as the stiffness modulus (a spring constant in one-dimension) of the radial glial fibers and the pial surface contained in the meninges surrounding the cerebellum since the cerebellar radius is proportional to its perimeter, r_0 as the preferred radius of the cerebellum, k_t denoting a growth potential due to cell proliferation, t_0 as thickness of the EGL (cortex), and, β quantified the mechanical resistance to changing the thickness of the EGL. Given our first assumption of an incompressible cerebellar core, we imposed the constraint

$$\frac{1}{2}\int d\theta\,(r-t)^2 = A_0,$$

with A_0 as a preferred cerebellar area. We applied the variational principle to minimize the energy functional subject to the core constraint, i.e.

$$\delta(E - \mu \int d\theta\,(r-t)^2) = 0,$$

where μ is a Lagrange multiplier. Assuming the preferred radius of the cerebellum is constant and the thickness of the EGL/cortex is also constant, then the preferred cerebellar shape was a circle and the EGL an annulus.

The variational analysis yielded the following equation of shape for t(θ);

$$\frac{d^2t}{d\theta^2} + q^2\,t(\theta) = \frac{k_t}{\beta}\left(t_0 + \frac{\frac{\mu r_0}{k_t}}{1-\frac{\mu}{k_r}}\right),$$

with $q^2 = \frac{k_t}{\beta}\left(1 + \frac{\frac{\mu}{k_t}}{1-\frac{\mu}{k_r}}\right)$. The solution to the equation of shape was

$$t(\theta) = A_t \sin(q\theta + \phi) + C_1(r_0, t_0, k_r, k_t, \mu),$$

595 with C_1 independent of θ and $A_t = \sqrt{2}\left(1-\frac{\mu}{k_r}\right)\sqrt{\frac{A_0}{\pi} - C_2(r_0, t_0, k_r, k_t, \mu)}$ such that $A_0 > \pi C_2$.

596 There was an additional equation of shape for r(θ) from the variational principle that depended

597 on t(θ) and so was determined

598 $$r(\theta) = -\frac{\frac{\mu}{k_r}}{1-\frac{\mu}{k_r}} A_t \sin(q\theta + \phi) + C_3(r_0, k_r, \mu).$$

599 We used the measured data at E16.5 to set the parameters to make predictions for the shape of

600 both the EGL and core (and so the relationship between the two) at later times. Plots assumed a

601 circular preferred shape, and with other parameters as follows: $\epsilon = \mu/k_r$ is shown in Fig. 5f, $c =$

602 $k_r/k_t = 0.06/\epsilon$, $A_t/r_0 = \epsilon/9.6$, $t_0/r_0 = \epsilon/4.8$, and $q = 6$. Note that for $\epsilon = 0.3$, these

603 parameters are numerically consistent with our E16.5 measurements: $A_t/t_0 =$

604 0.5 and $r_0/t_0 = 16$, as well as the observed number of invaginations in the half circle: $q/2 = 3$.

605 All of these parameters are either constant or depend on the time-like parameter ϵ. One of these

606 dependencies has a functional form that is physically justifiable ($A_t \sim \epsilon$), another has a form that

607 is biologically justifiable ($c \sim 1/\epsilon$), owing to the decrease in the number of radial glia over time.

608

609 We defined a dimensionless "shape factor" as half of the perimeter divided by the square root of

610 half of the area as appropriate for a semi-circle. To compare the model's predictive deviation of

611 this quantity form the semi-circular value we assumed a linear relationship between ϵ and time t

612 measured in embryonic days: $\epsilon(t) = 0.3(t-15.5)$.

613

614 **Statistical analyses**

615 Statistical analyses were performed using Matlab software. Significance was determined at P<

616 0.05. Two-way ANOVA was used for proliferation analysis as two variables were tracked,

mouse and region. Cell shape, volume, fiber distribution, EGL thickness and bulk modulus were run under a standard ANOVA. After ANOVA analysis a multiple comparison was run with Tukey's honestly significant difference criterion. F-test for variance and two-tailed student's paired t-test were used for slice cutting and relaxation quantifications. The degrees of freedom, where appropriate, and P values are given in the figure legends. All error bars are standard deviations. No statistical methods were used to predetermine the sample sizes. We used sample sizes aligned with the standard in the field. No randomization was used nor was data collection or analysis performed blind.

Data Availability

Data that support the findings of this study are available from the corresponding authors upon reasonable request.

Supplemental Movie Text

Movie S1: Live slice cutting and relaxation reveals circumferential tension along the EGL. Time-lapse movie shows relaxation of live tissue slice after cutting radially through the EGL and into the underlying core. Images were acquired every 10 seconds for 10 minutes. The time-lapse was started moments after the tissue was collected in frame after the cut. The slice shown in the video is the same as in Fig.2 f-h.

Movie S2: Live slice cutting and relaxation reveals radial tension between the EGL and The VZ. Time-lapse movie shows relaxation of live tissue slice after cutting horizontally into the core between the EGL and the VZ. Images were acquired every 10 seconds for 10 minutes. The

640 time-lapse was started moments after the tissue was collected in frame after the cut. The Slice
641 shown in the video is the same as in Fig. 4c-e.
642
643 **Movie S3**: Live slice imaging reveals fluid-like behavior in the EGL. Time-lapse movie shows
644 dynamic cell rearrangement of progenitors within the EGL. Image stacks were acquired every
645 ~3.5 minutes for 5 hours. Cells undergo mixing and neighbor exchange in the tens to hundreds of
646 minutes.
647
648 **Movie S4**: Live slice imaging reveals fluid-like behavior in the EGL. Time-lapse shown in
649 Movie S3, with a subset of cells tracked through time and their positions marked with colored
650 spheres.

References:

1. Tallinen T, Chung JY, Biggins JS, Mahadevan L. Gyrification from constrained cortical expansion. Proc Natl Acad Sci U S A. 2014;111(35):12667-72.
2. Ronan L, Voets N, Rua C, Alexander-Bloch A, Hough M, Mackay C, et al. Differential tangential expansion as a mechanism for cortical gyrification. Cereb Cortex. 2014;24(8):2219-28.
3. Bayly PV, Okamoto RJ, Xu G, Shi Y, Taber LA. A cortical folding model incorporating stress-dependent growth explains gyral wavelengths and stress patterns in the developing brain. Phys Biol. 2013;10(1):016005.
4. Xu G, Knutsen AK, Dikranian K, Kroenke CD, Bayly PV, Taber LA. Axons pull on the brain, but tension does not drive cortical folding. J Biomech Eng. 2010;132(7):071013.
5. Hohlfeld E, Mahadevan L. Unfolding the sulcus. Phys Rev Lett. 2011;106(10):105702.
6. Bayly PV, Taber LA, Kroenke CD. Mechanical forces in cerebral cortical folding: a review of measurements and models. J Mech Behav Biomed Mater. 2014;29:568-81.
7. Lejeune E, Javili A, Weickenmeier J, Kuhl E, Linder C. Tri-layer wrinkling as a mechanism for anchoring center initiation in the developing cerebellum. Soft Matter. 2016;12(25):5613-20.
8. Karzbrun E, Kshirsagar A, Cohen SR, Hanna JH, Reiner O. Human Brain Organoids on a Chip Reveal the Physics of Folding. Nature physics. 2018;14(5):515-22.
9. Tallinen T, Chung JY, Rousseau F, Girard N, Lefèvre J, Mahadevan L. On the growth and form of cortical convolutions. Nature Physics. 2016;12:588-93.
10. Engstrom TA, Zhang T, Lawton AK, Joyner AL, Schwarz JM. Buckling without Bending: A New Paradigm in Morphogenesis. Phys Rev X. 2018;8(4).
11. Leto K, Arancillo M, Becker EB, Buffo A, Chiang C, Ding B, et al. Consensus Paper: Cerebellar Development. Cerebellum. 2016;15(6):789-828.
12. Legue E, Riedel E, Joyner AL. Clonal analysis reveals granule cell behaviors and compartmentalization that determine the folded morphology of the cerebellum. Development. 2015;142(9):1661-71.
13. Legue E, Gottshall JL, Jaumouille E, Rosello-Diez A, Shi W, Barraza LH, et al. Differential timing of granule cell production during cerebellum development underlies generation of the foliation pattern. Neural Dev. 2016;11(1):17.
14. Sudarov A, Joyner AL. Cerebellum morphogenesis: the foliation pattern is orchestrated by multi-cellular anchoring centers. Neural Dev. 2007;2:26.
15. Richman DP, Stewart RM, Hutchinson JW, Caviness VS, Jr. Mechanical model of brain convolutional development. Science. 1975;189(4196):18-21.
16. Nelson CM. On Buckling Morphogenesis. J Biomech Eng. 2016;138(2):021005.
17. Hannezo E, Prost J, Joanny JF. Mechanical instabilities of biological tubes. Phys Rev Lett. 2012;109(1):018101.
18. Shyer AE, Tallinen T, Nerurkar NL, Wei Z, Gil ES, Kaplan DL, et al. Villification: how the gut gets its villi. Science. 2013;342(6155):212-8.
19. Wiggs BR, Hrousis CA, Drazen JM, Kamm RD. On the mechanism of mucosal folding in normal and asthmatic airways. J Appl Physiol (1985). 1997;83(6):1814-21.
20. Szulc KU, Lerch JP, Nieman BJ, Bartelle BB, Friedel M, Suero-Abreu GA, et al. 4D MEMRI atlas of neonatal FVB/N mouse brain development. Neuroimage. 2015;118:49-62.

21. Mota B, Herculano-Houzel S. BRAIN STRUCTURE. Cortical folding scales universally with surface area and thickness, not number of neurons. Science. 2015;349(6243):74-7.
22. Allen HG. Analysis and design of structural sandwich panels. 1st ed. Oxford, New York,: Pergamon Press; 1969. xvi, 283 p. p.
23. Zhao R, Zhao X. Multimodal Surface Instabilities in Curved Film–Substrate Structures. Journal of Applied Mechanics. 2017;84(8):081001--13.
24. Budday S, Sommer G, Haybaeck J, Steinmann P, Holzapfel GA, Kuhl E. Rheological characterization of human brain tissue. Acta Biomater. 2017;60:315-29.
25. Mammoto T, Ingber DE. Mechanical control of tissue and organ development. Development. 2010;137(9):1407-20.
26. Harding MJ, McGraw HF, Nechiporuk A. The roles and regulation of multicellular rosette structures during morphogenesis. Development. 2014;141(13):2549-58.
27. Stemple DL. Structure and function of the notochord: an essential organ for chordate development. Development. 2005;132(11):2503-12.
28. He B, Doubrovinski K, Polyakov O, Wieschaus E. Apical constriction drives tissue-scale hydrodynamic flow to mediate cell elongation. Nature. 2014;508(7496):392-6.
29. Leung AW, Li JYH. The Molecular Pathway Regulating Bergmann Glia and Folia Generation in the Cerebellum. Cerebellum. 2018;17(1):42-8.
30. Yuasa S. Bergmann glial development in the mouse cerebellum as revealed by tenascin expression. Anat Embryol (Berl). 1996;194(3):223-34.
31. Yamada K, Watanabe M. Cytodifferentiation of Bergmann glia and its relationship with Purkinje cells. Anat Sci Int. 2002;77(2):94-108.
32. Van Essen DC. A tension-based theory of morphogenesis and compact wiring in the central nervous system. Nature. 1997;385(6614):313-8.
33. Li K, Leung AW, Guo Q, Yang W, Li JY. Shp2-dependent ERK signaling is essential for induction of Bergmann glia and foliation of the cerebellum. The Journal of neuroscience : the official journal of the Society for Neuroscience. 2014;34(3):922-31.
34. Sillitoe RV, Joyner AL. Morphology, molecular codes, and circuitry produce the three-dimensional complexity of the cerebellum. Annual review of cell and developmental biology. 2007;23:549-77.
35. Rahimi-Balaei M, Afsharinezhad P, Bailey K, Buchok M, Yeganeh B, Marzban H. Embryonic stages in cerebellar afferent development. Cerebellum Ataxias. 2015;2:7.
36. Gotz M, Hartfuss E, Malatesta P. Radial glial cells as neuronal precursors: a new perspective on the correlation of morphology and lineage restriction in the developing cerebral cortex of mice. Brain Res Bull. 2002;57(6):777-88.
37. Reillo I, de Juan Romero C, Garcia-Cabezas MA, Borrell V. A role for intermediate radial glia in the tangential expansion of the mammalian cerebral cortex. Cereb Cortex. 2011;21(7):1674-94.
38. Hansen DV, Lui JH, Parker PR, Kriegstein AR. Neurogenic radial glia in the outer subventricular zone of human neocortex. Nature. 2010;464(7288):554-61.
39. Heng X, Guo Q, Leung AW, Li JY. Analogous mechanism regulating formation of neocortical basal radial glia and cerebellar Bergmann glia. Elife. 2017;6.
40. Nowakowski TJ, Pollen AA, Sandoval-Espinosa C, Kriegstein AR. Transformation of the Radial Glia Scaffold Demarcates Two Stages of Human Cerebral Cortex Development. Neuron. 2016;91(6):1219-27.

742 41. Andersen BB, Korbo L, Pakkenberg B. A quantitative study of the human cerebellum
743 with unbiased stereological techniques. The Journal of comparative neurology.
744 1992;326(4):549-60.
745 42. Machold R, Fishell G. Math1 is expressed in temporally discrete pools of cerebellar
746 rhombic-lip neural progenitors. Neuron. 2005;48(1):17-24.
747 43. Isaka F, Ishibashi M, Taki W, Hashimoto N, Nakanishi S, Kageyama R. Ectopic
748 expression of the bHLH gene Math1 disturbs neural development. Eur J Neurosci.
749 1999;11(7):2582-8.
750 44. Muzumdar MD, Tasic B, Miyamichi K, Li L, Luo L. A global double-fluorescent Cre
751 reporter mouse. Genesis. 2007;45(9):593-605.
752 45. Daigle TL, Madisen L, Hage TA, Valley MT, Knoblich U, Larsen RS, et al. A Suite of
753 Transgenic Driver and Reporter Mouse Lines with Enhanced Brain-Cell-Type Targeting
754 and Functionality. Cell. 2018;174(2):465-80 e22.
755 46. Wojcinski A, Lawton AK, Bayin NS, Lao Z, Stephen DN, Joyner AL. Cerebellar granule
756 cell replenishment postinjury by adaptive reprogramming of Nestin(+) progenitors. Nat
757 Neurosci. 2017;20(10):1361-70.
758 47. Rohrbach D, Lloyd HO, Silverman RH, Mamou J. Fine-resolution maps of acoustic
759 properties at 250 MHz of unstained fixed murine retinal layers. J Acoust Soc Am.
760 2015;137(5):EL381-7.
761 48. Rohrbach D, Silverman RH, Chun D, Lloyd HO, Urs R, Mamou J. Improved High-
762 Frequency Ultrasound Corneal Biometric Accuracy by Micrometer-Resolution Acoustic-
763 Property Maps of the Cornea. Transl Vis Sci Technol. 2018;7(2):21.

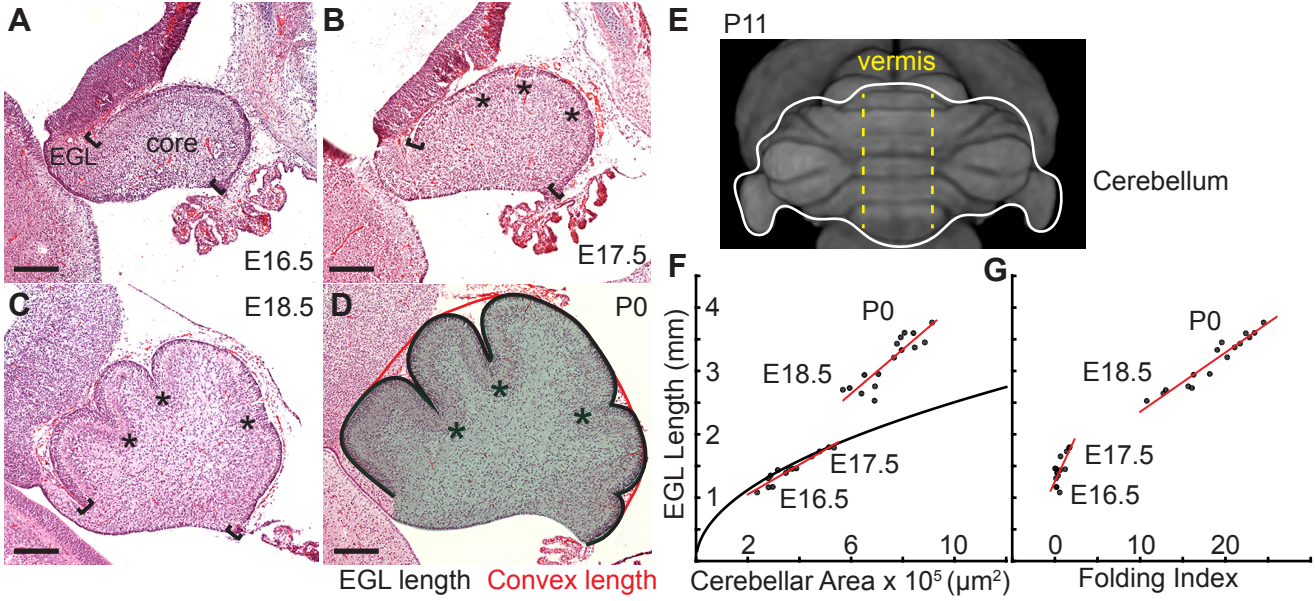

Fig. 1. Initiation of cerebellar folding correlates with timing of differential expansion. (A-D), H&E stained midline sagittal sections of FVB/N mice at the indicated embryonic (E) and postnatal days (P). Anterior to the left. Stars: ACs. Brackets: anterior/posterior ends of the EGL. Black line and red line in (D): EGL and convex length, respectively. Shaded area: core. (E) manganese enhanced magnetic resonance imaging of P11 cerebellum outlined in white adapted from (20). Anterior to the top. Vermis indicated by dotted yellow lines. (F), At E16.5 and E17.5 expansion of EGL length and cerebellar area fit the proportional expansion of a semi-circle (curve). At E18.5 and P0 EGL expansion is greater than core area growth creating differential expansion. (G), Folding index [1 - (convex length/EGL length) x 100] reveals folding initiates during differential expansion. Scale bars: 200 μm.

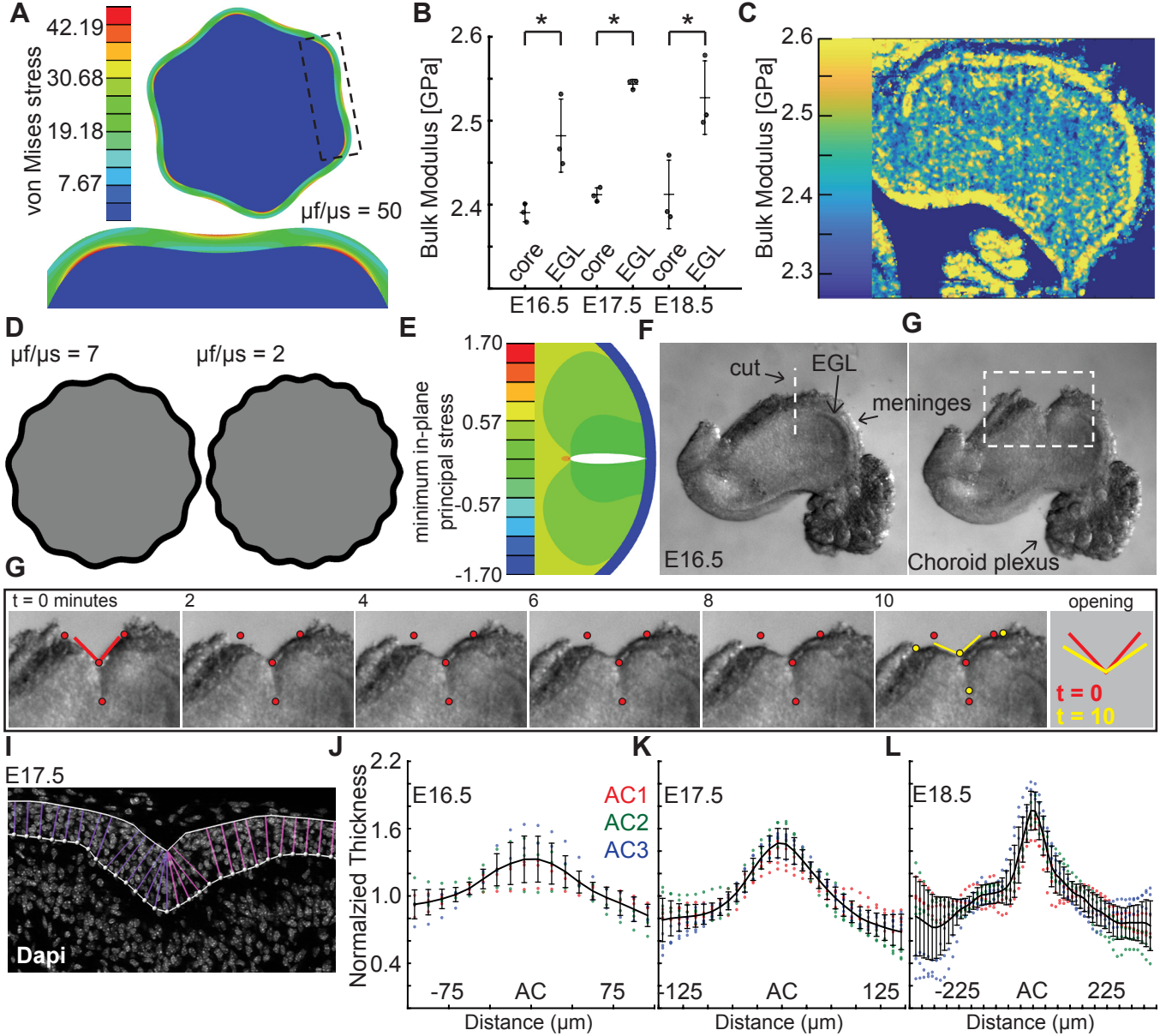

Fig. 2. Measured tissue stiffness, stress, and shape at folding initiation are inconsistent with wrinkling models. (A), Inducing the correct number of folds through a wrinkling model requires a stiffness differential between the layers of 50 fold (μf/μs = 50, g = 1.05). (B,C) Acoustic mapping of cerebellar slices show a slightly stiffer EGL than core at each stage (anova df = 5; P = $1.0e^{-4}$ F = 13.59), but not the required differential. Stars indicate statistical differences. (D) Wrinkling simulations constrained by developmental data produce wavelengths inconsistent with the embryonic mouse cerebellum. (E) Elastoc simulations predict the EGL remains closed after cutting. (F,G) Images of a live cerebellar slice before and after cutting, and images from time lapse movie, (H) show the EGL opens, revealing circumferential tension along the EGL. Red and yellow dots: cut edges. Lines: relaxation angle. (I) Staining of nuclei with EGL outlined and lines used to measure thickness. (J-L) Normalized EGL thickness (thickness/mean thickness) at the ACs increases during folding initiation (anova E16.5 df = 29, P = $8.2e^{-20}$ F = 12.59. E17.5 df = 29, P = $3.4e^{-116}$ F = 62.78, E18.5 df = 57, P = $6.8e^{-67}$ F = 13.28). At E16.5 only brains with visible ACs were included. Error bars: S.D.

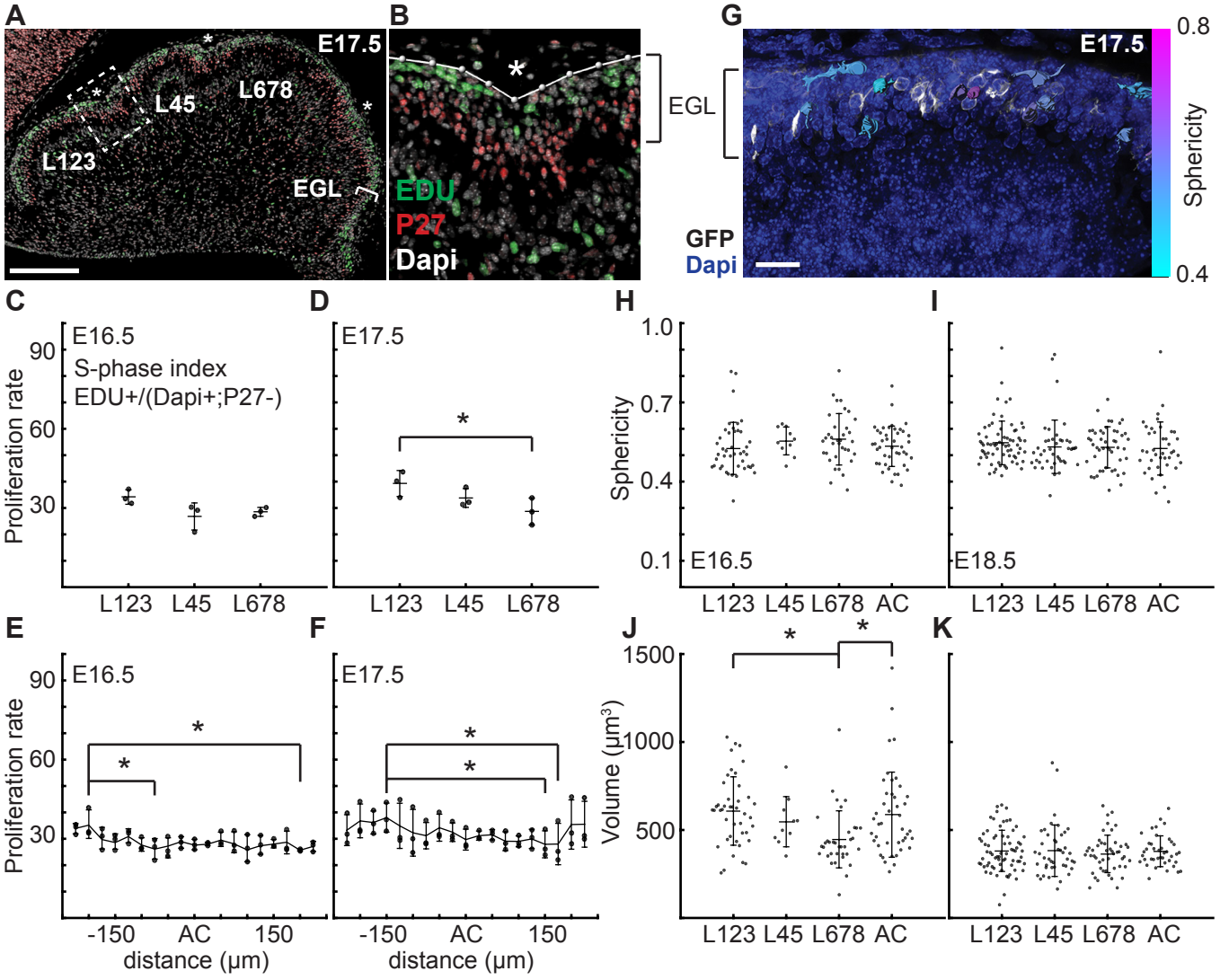

Fig. 3. At folding initiation the EGL has uniform proliferation, cell size, and cell shape. (A,B) Low and high power images of immuno-histochemical (IHC) staining of sagittal cerebellar sections to measure proliferation in the lobules (L) indicated at 25 µm windows surrounding the ACs (stars). Scale bar: 200 µm. (C,D) EGL proliferation rates are shown before and during the onset of invagination (Two-way anova: df = 2. (C) P = 0.10, F = 4.36 (D) P = 0.03, F = 10.31). (E,F) Proliferation rates are shown in the AC and in the surrounding EGL showing uniformity (Two-way anova: df = 18. (E) P = 0.03, F = 2.15 (F) P =2.1e^{-3} F = 3.06). (G) Section of *Atoh1-CreER/+; R26*$^{MTMG/+}$ E16.5 cerebellum showing masked labeled cells. Scale bar: 20 µm. (H,I) Cell shape (sphericity) measurements before and during folding (anova df = 3. (H) P = 0.34, F = 1.13 i P = 0.61,F = 0.61). (J,K) Cell size measuements before and during folding (anova df = 3. (J) P =3.6e^{-3} F = 4.75 , (K) P = 0.85, F = 0.26). Stars indicate statistical differences. Error bars: S.D.

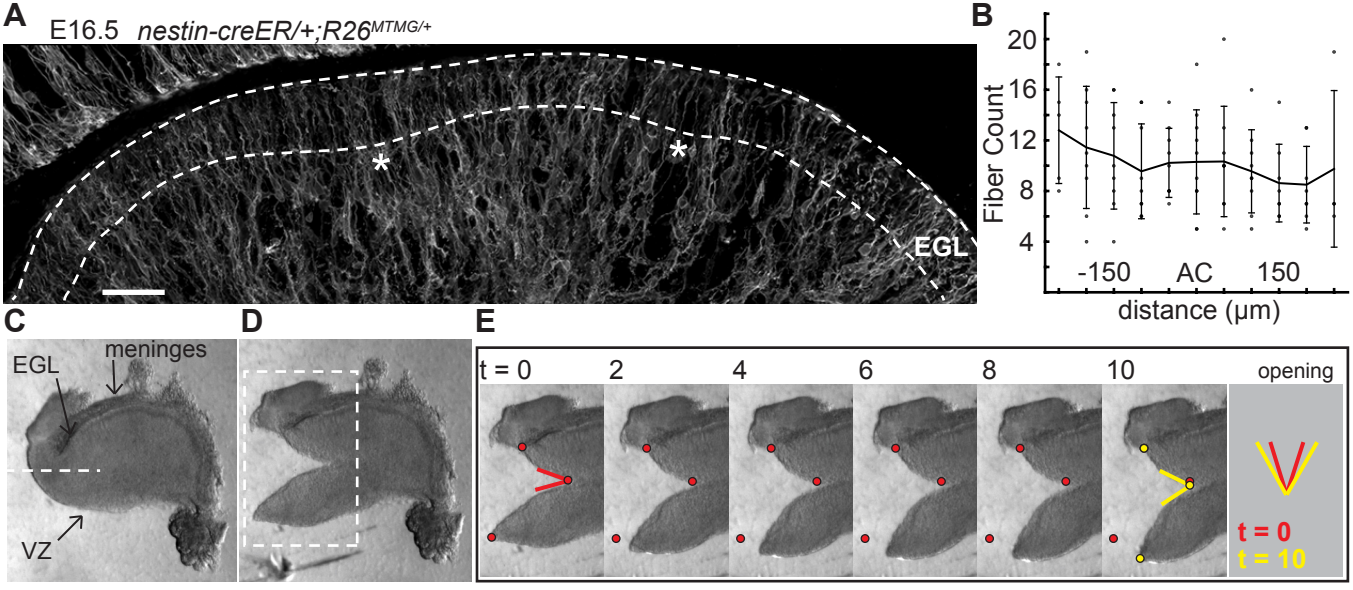

Fig. 4. The EGL has a uniform distribution of crossing fibers at folding initiation. (A) E16.5 *nestin-CreER/+; R26*$^{MT-MG/+}$ cerebellum section showing flourescent labeling of radial and Bergmann glial fibers. Stars: AC. Dotted lines denote EGL. Scale bar: 50 µm. (B) Measurements of fiber density in the ACs compared to the surrounding EGL (anova df = 10; P = 0.76, F = 0.66). Error bars: S.D. (C-E) Still images of a tissue cutting experiment to test for radial tension between the EGL and the VZ. Red and yellow dots: cut edges at t = 0, 10. Lines: relaxation angle.

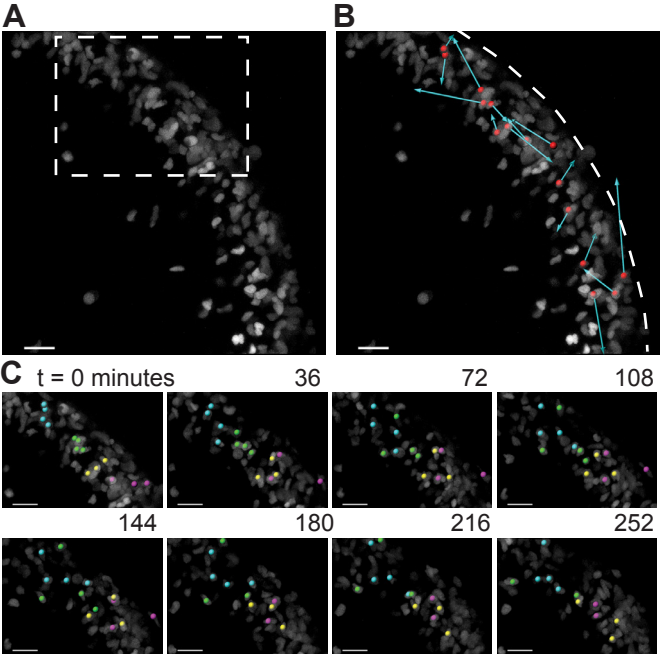

Fig. 5. During folding initiation, cells within the EGL are motile and undergo rearrangement. (A) Image of E16.5 live cerebellar slice (*Atoh1-creER/+ R26*$^{Ai75/+}$) showing scattered labeling within the EGL. (B) Red dots indicate starting position, displacement arrows show final position of marked cells after 5 hours. White dashed line indicates outer edge of EGL. (C) Still images from timelapse, inset above. Cells tracked and marked with colored spheres exchange nearest neighbors over a time-scale of tens of minutes. Scale bars are 20 μm.

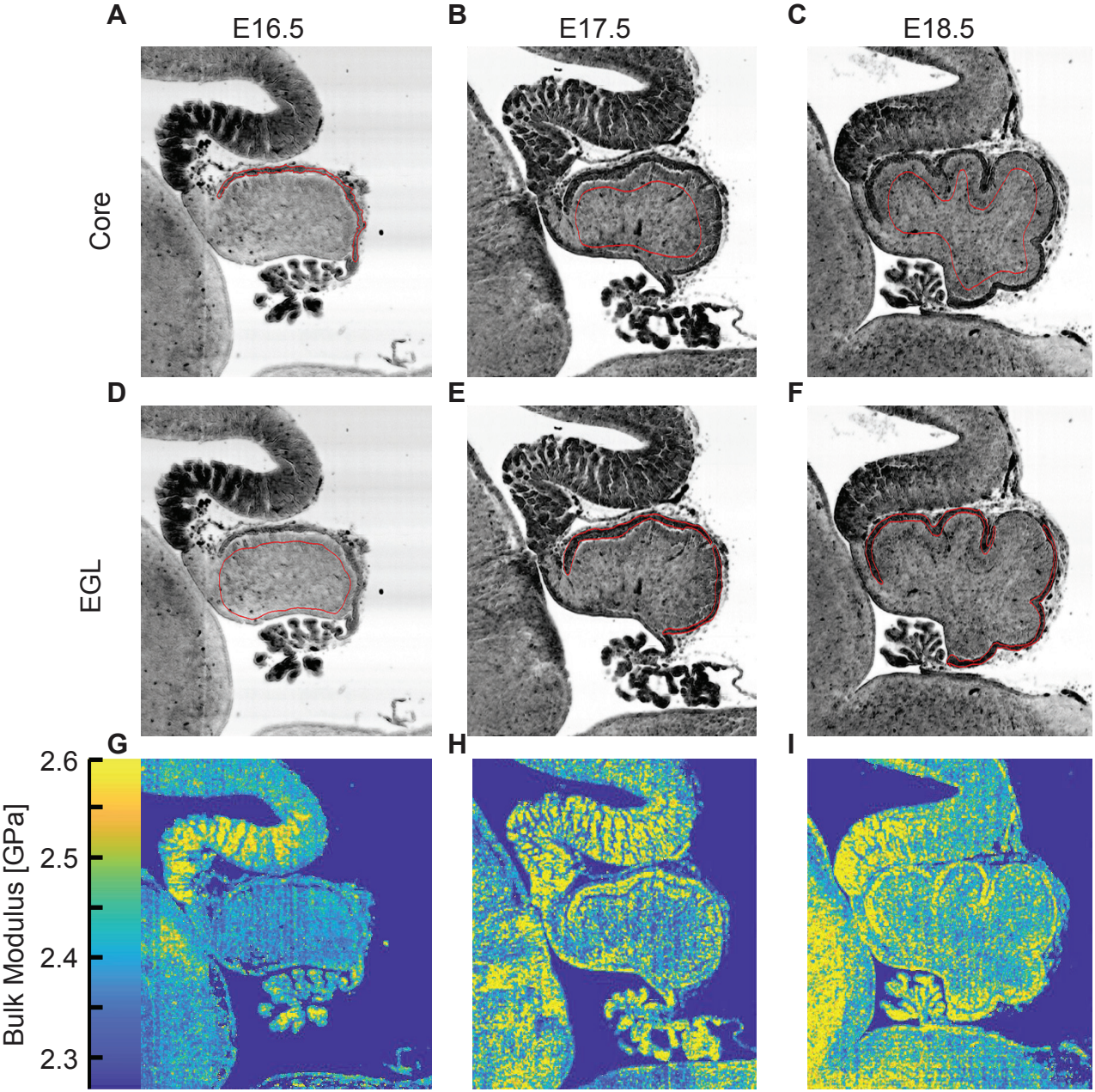

Fig. S1. Examples of the regions measured regions by acoustic microscopy. (A-F) Examples of the Region of Interest (ROI) measured for each for core and EGL. (H-J), Representative bulk modulus maps.

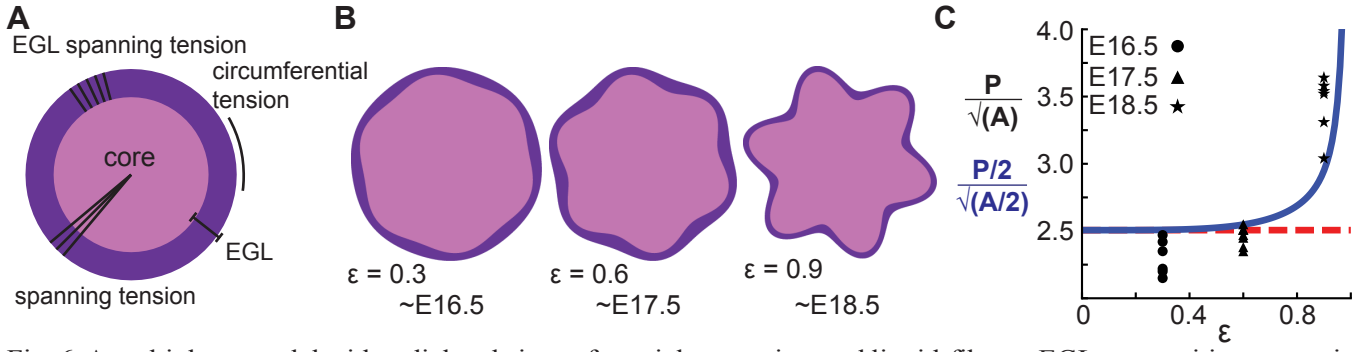

Fig. 6. A multiphase model with radial and circumferential constraints and liquid-fibrous EGL composition approximates evolution of cerebellar shape. (A) Schematic of multiphase model showing types of tension. (B) Thickness variations that arise concomitant with folding approximate those seen in the cerebellum. (C) Shape factor analysis: model for semicircle (red), multi-phase model shape prediction (blue) and actual shape measured from sections (black). Assumed linear relationship between ε and time, $\varepsilon(t) = 0.3(t - 15.5)$.

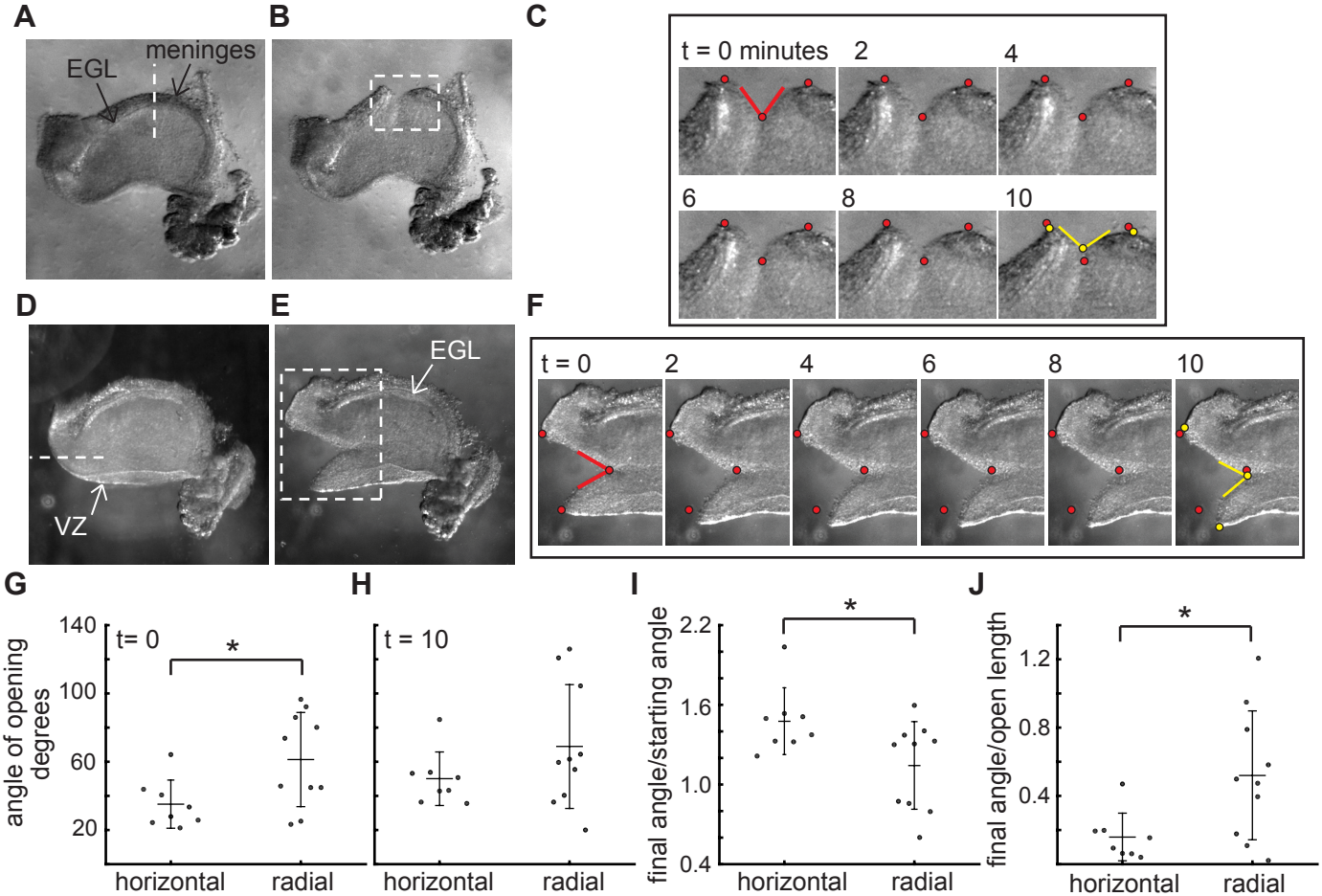

Fig. S2. The stress patterns within the cerebellum are different between the EGL and the VZ. (A-C), Example of a live cerebellar slice before (A) and after (B) a radial cut through the EGL, and still images from a time-lapse (C). Time = 0 minutes is at the time it takes to remove the knife and start the imaging, therefore the cut has already begun opening. (D-F) Example of a live cerebellar slice before (D) and after (E) a horizontal cut through between the EGL and ventricular zone (VZ), and still images from a movie (F). (G-I) radial cuts through the EGL open more quickly initially than horizontal cuts between the EGL and the Ventricular zone, but the latter continue to relax for longer ((G) f-test for unequal varience P = 0.09, two tailed t-test df = 16, p = 0.03, T = -2.43; (H) f-test P = 0.04 and unequal varience two-tailed t-test df = 12.8 P = 0.16, T = -1.48; (I) f-test P = 0.49 and two tailed t-test df = 16, P = 0.03, T = 2.43). (J) The degree of opening is tightly related to the length of the opening in horizontal cuts but not in radial cuts (f-test P = 0.02, unequal varience two tailed t-test df = 11.89, P = 0.02, T = -2.80). Stars: statistical differences. Error bars: S.D.

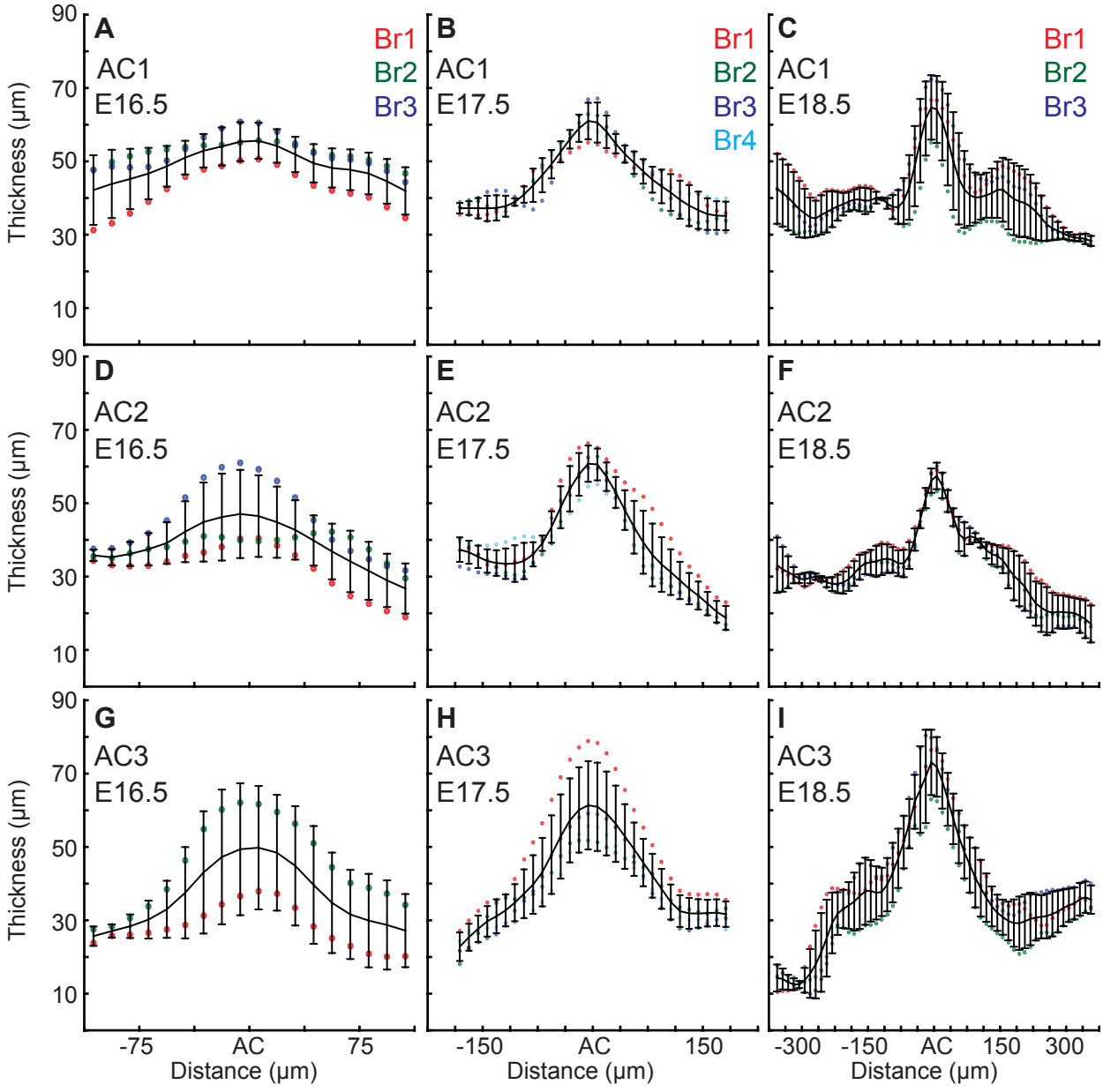

Fig. S3. EGL thickness in the ACs during the initiation of folding. Only E16.5 cerebella that showed regional thickening in the geometry where ACs normally arise were used for the measurements, and one embryo did not yet have an AC3. (A-C) Thickness variation in and surrounding AC1 (anova (A) df = 17, P = 0.13, F = 1.55 (B) df = 29, P = $7.0e^{-14}$ F = 6.82 (C) df = 57, P = $9.1e^{-11}$ F = 4.05). (D-F) Thickness variation in and surrounding AC2 (anova (D) df = 17, P = 0.08 F = 1.74 (E) df = 29 P = 3.9^{e-22} F = 11.88 (F) df = 57 P = $2.9e^{-35}$ F = 16.35). (G-I) Thickness variation in and surrounding AC3 (anova (G) df = 17, P = 0.59 F = 0.89 (H) df = 29, P = $2.4e^{-17}$ F = 9.81 (I) df = 57, P = $7.6e^{-33}$ F = 14.57). Error bars are S.D.

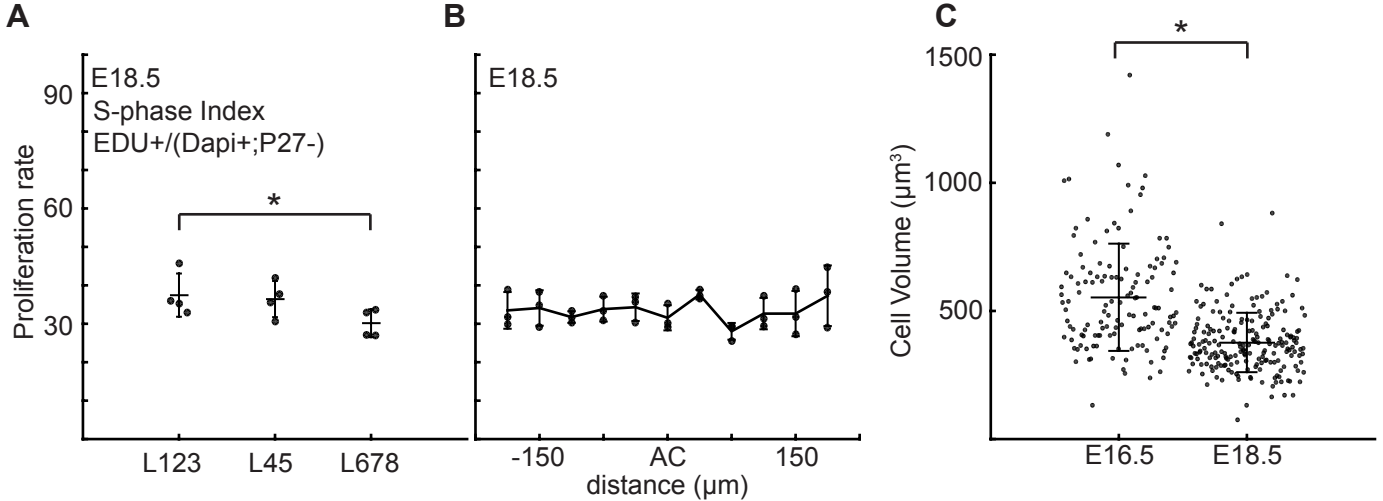

Fig. S4. Proliferation rate is reduced in the central zone of the cerebellum after folding initiation. (A) Proliferation is reduced in lobule region L678 compared to other lobules (anova: df = 2; P = 0.01, F = 9.24). (B) Proliferation through the AC regions is uniform with the surrounding EGL (anova: df = 10; P = 0.17, F = 1.64). (C) At E18.5 cells within the EGL are smaller than at earlier stages (two-tailed t-test df = 330 P = $2.92e^{-20}$, T = 9.85). Stars: statistical differences. Error bars: S.D.

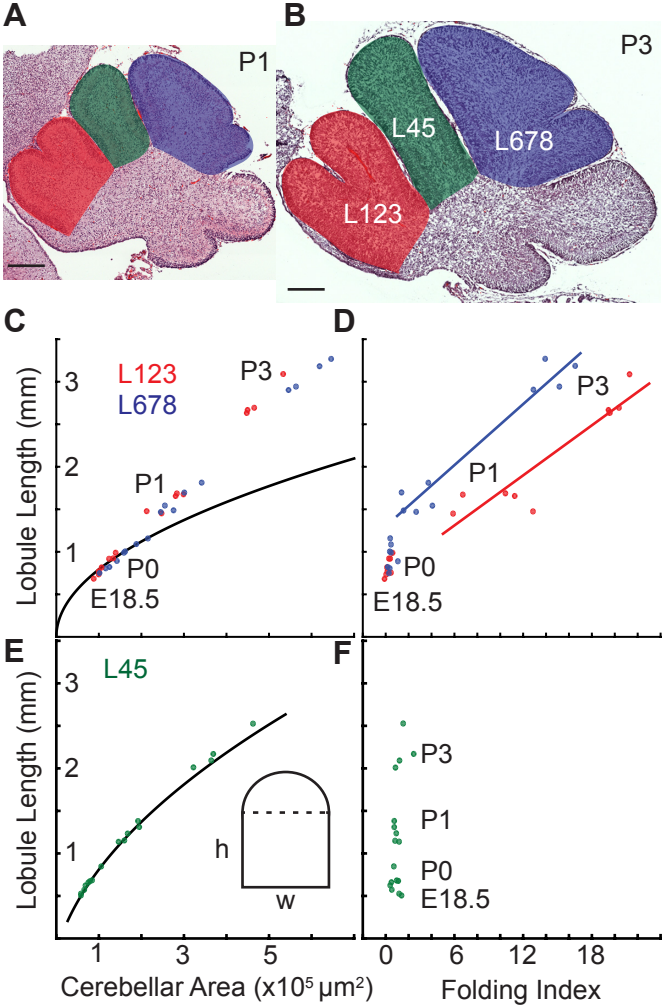

Fig. S5. Differential expansion correlates with progressive subfolding of initial folds. (A,B) H&E stained midline sagittal sections of FVB/N cerebella at P1 and P3 with three lobule regions highlighted in red (L123), green (L45), and blue (L678). (C) Expansion of lobule length and lobule area for L123 and L678 approximate the proportional expansion of a semi-circle (curve) in both regions at E18.5 and P0. After P0 the EGL expansion in both regions increases more than the underlying area creating differential expansion. (D) Folding initiates during regional differential expansion. (E) The expansion in length and area of L45 is proportional to a columnar shape (curve and inset figure) from E18.5 to P3. (F) the L45 region remains unfolded through P3. Scale bars: 200 μm.

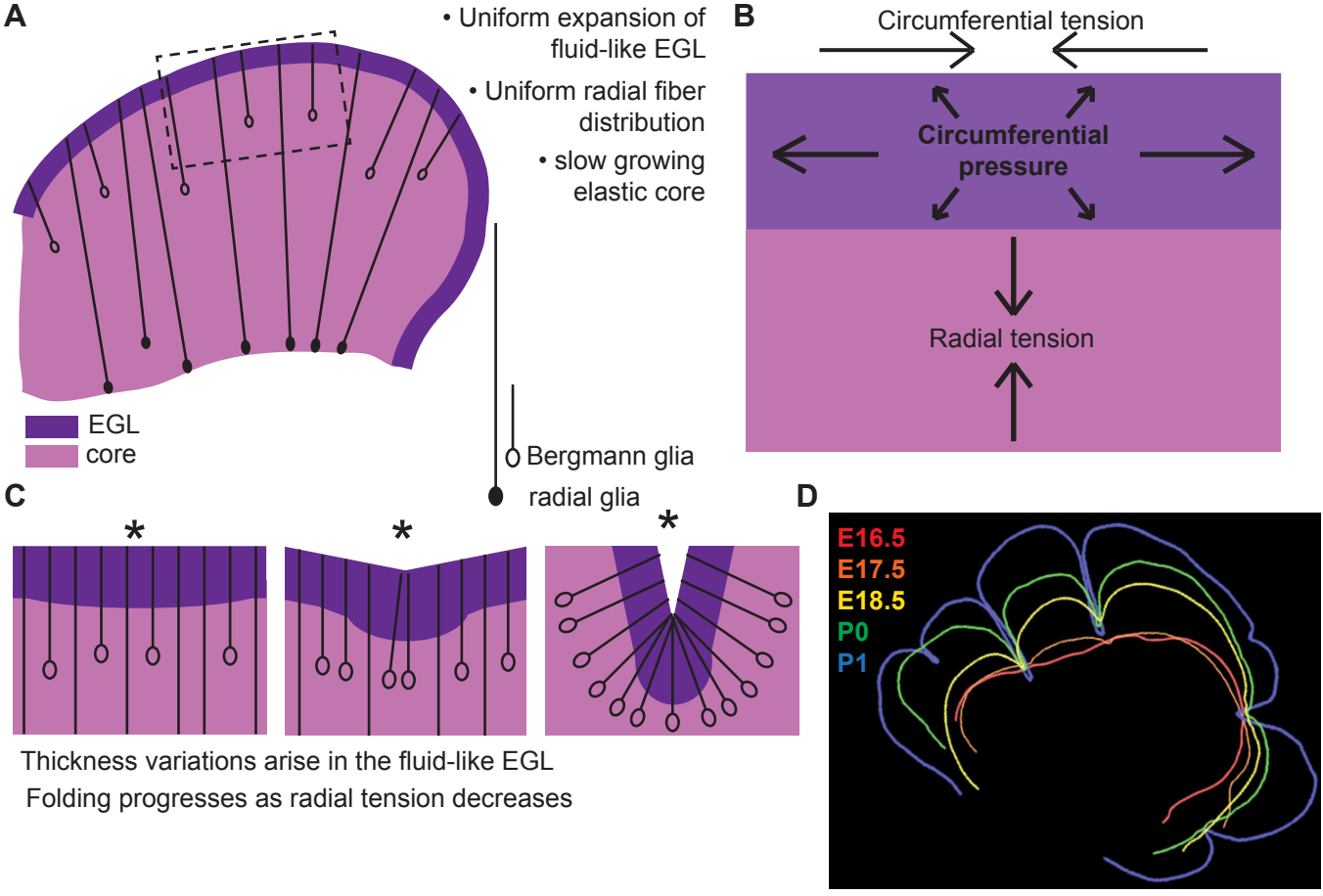

Fig. S6. Uniform cell behaviors within a fluid-like EGL create differential expansion based folding approximated by a multiphase model with radial and circumferential tension. (A) Cartoon of E16.5 cerebellum showing the EGL (dark purple) overlying the in incompressible core (light purple) with fibers (lines) of radial glia (closed ovals) and Bergmann glia (open ovals) crossing the cerebellum and the EGL. (B) Map of stress within the cerebellum at the onset of foliation. (C) Schematics showing that an AC is first detected as a regional inward thickening of the EGL (left). The constraining tensions shape the fluid-like EGL such that the EGL becomes thicker at the AC (middle). As radial glia transition to Bergmann glia, modeling predicts a reduction in radial tension (right). (D) Since ACs hold their position in space, and compartmentalize the cells within the EGL, we propose that they behave as mechanical boundaries allowing local domains of differential expansion to arise and progressive folding to occur.